

ALMA DETECTION OF INTERSTELLAR METHOXYMETHANOL (CH₃OCH₂OH)

BRETT A. MCGUIRE,^{1,2,*} CHRISTOPHER N. SHINGLEDECKER,³ ERIC R. WILLIS,³ ANDREW M. BURKHARDT,⁴
SAMER EL-ABD,⁴ ROMAN A. MOTIYENKO,⁵ CRYSTAL L. BROGAN,¹ TODD R. HUNTER,¹ LAURENT MARGULÈS,⁵
JEAN-CLAUDE GUILLEMIN,⁶ ROBIN T. GARROD,^{3,4} ERIC HERBST,^{3,4} AND ANTHONY J. REMIJAN¹

¹*National Radio Astronomy Observatory, Charlottesville, VA 22903, USA*

²*Harvard-Smithsonian Center for Astrophysics, Cambridge, MA 02138, USA*

³*Department of Chemistry, University of Virginia, Charlottesville, VA 22903, USA*

⁴*Department of Astronomy, University of Virginia, Charlottesville, VA 22903, USA*

⁵*Laboratoire de Physique des Lasers, Atomes, et Molécules, UMR CNRS 8523, Université de Lille I, F-59655 Villeneuve d'Ascq Cédex, France*

⁶*Institut des Sciences Chimiques de Rennes, Ecole Nationale Supérieure de Chimie de Rennes, CNRS, UMR 6226, 11 Allée de Beaulieu, CS 50837, 35708 Rennes Cedex 7, France*

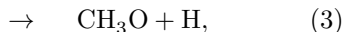
ABSTRACT

We report the detection of interstellar methoxymethanol (CH₃OCH₂OH) in ALMA Bands 6 and 7 toward the MM1 core in the high-mass star-forming region NGC 6334I at $\sim 0.1'' - 1''$ spatial resolution. A column density of $4(2) \times 10^{18} \text{ cm}^{-2}$ at $T_{\text{ex}} = 200 \text{ K}$ is derived toward MM1, ~ 34 times less abundant than methanol (CH₃OH), and significantly higher than predicted by astrochemical models. Probable formation and destruction pathways are discussed, primarily through the reaction of the CH₃OH photodissociation products, the methoxy (CH₃O) and hydroxymethyl (CH₂OH) radicals. Finally, we comment on the implications of these mechanisms on gas-phase vs grain-surface routes operative in the region, and the possibility of electron-induced dissociation of CH₃OH rather than photodissociation.

Keywords: Astrochemistry, ISM: molecules, ISM: individual objects (NGC 6334I)

1. INTRODUCTION

Given its high abundance in the interstellar medium (ISM), the photodissociation of methanol (CH_3OH) – producing the methyl (CH_3), hydroxymethyl (CH_2OH), and methoxy radicals (CH_3O) – is one of the most dominant sources of reactive organic species driving interstellar chemical evolution. The branching ratio for these reactions,



is a topic of considerable interest, both in the laboratory and in astrochemical models (Laas et al. 2011). These ratios are difficult to experimentally constrain, however, given that CH_2OH and CH_3O are indistinguishable by mass spectroscopic techniques, and gas-phase production rates are low enough that direct detection by rotational spectroscopy is challenging (Laas et al. 2013). There is also a question of the relative importance of these branching ratios in gas-phase vs grain-surface chemistry (Laas et al. 2011). The observation of interstellar species which are likely to be products of one or more of these radicals, and insight into its formation in either the gas or solid phase (or both), is highly desirable.

One such highly-desirable target is methoxymethanol ($\text{CH}_3\text{OCH}_2\text{OH}$), which is thought to form primarily through either the direct reaction of CH_3O with CH_2OH in the solid-phase (Garrod et al. 2008):



or via an $\text{O}(^1\text{D})$ insertion into dimethyl ether (CH_3OCH_3). Although CH_3O has been detected in the ISM (Cernicharo et al. 2012), CH_2OH has proven elusive, making it difficult to accurately incorporate into chemical models. If $\text{CH}_3\text{OCH}_2\text{OH}$ does form through Reaction 4, and the rate can be reliably measured in the laboratory, observation of the species in the ISM would therefore provide quantitative insight into the presence of CH_2OH , even without its direct detection.

Observation of $\text{CH}_3\text{OCH}_2\text{OH}$ would therefore provide much-needed constraints on the branching ratios for Reactions 1, 2, and 3, if $\text{CH}_3\text{OCH}_2\text{OH}$ can be determined to have a grain-surface formation pathway.

Here, we present the first interstellar detection of $\text{CH}_3\text{OCH}_2\text{OH}$ using ALMA data in Bands 6 and 7 toward NGC 6334I, a massive protocluster (Hunter et al. 2006) currently forming numerous massive stars and harboring two distinct regions of hot core line emission (MM1 and MM2, Brogan et al. 2016; Zernickel et al.

2012) at a distance of 1.3 kpc (Reid et al. 2014). The observations are detailed in §2, and the spectroscopy in §3. In §4 the results are presented and analyzed, and in §5, the formation and destruction chemistry for $\text{CH}_3\text{OCH}_2\text{OH}$ is explored in the context of the detection.

2. OBSERVATIONS

We present detections of the $\text{CH}_3\text{OCH}_2\text{OH}$ molecule in four ALMA datasets. The salient observing and imaging parameters are presented in Table 1. The Cycle 3 data (observed in 2016) were calibrated by the ALMA Cycle 4 pipeline (CASA 4.7.2) as described in Hunter et al. (2017), and the Cycle 4 data (observed in 2017) were calibrated by the ALMA Cycle 5 pipeline (CASA 5.1.1). For each dataset, the (relatively) line-free continuum channels were carefully selected and used to construct an initial continuum image model that was then used to iteratively self-calibrate the data. The same channels were also used to subtract the continuum emission in the uv-plane before the spectral cubes were imaged. The data presented here have been corrected for primary beam attenuation.

3. SPECTROSCOPY

The rotational spectra of two conformers of $\text{CH}_3\text{OCH}_2\text{OH}$ were recently published by Motiyenko et al. (2017) between 150 and 450 GHz. The detection of the lower energy conformer, Conformer I, is reported here. The dipole moment components determined in that study at the MP2/aug-cc-pVTZ level of theory and basis set were small ($\mu_a = 0.22$ D, $\mu_b = 0.08$ D, $\mu_c = 0.13$ D). A careful analysis of the relative intensities of A- and C-type lines in the laboratory spectrum, by a subset of the authors, showed that better agreement with corresponding relative intensities in the calculated spectrum was obtained by scaling the value of μ_c to 0.11 D. We have therefore adopted this value for this work. The overall RMS deviation of the fit was reported to be 40 kHz, corresponding to ~ 0.04 km s⁻¹ at these frequencies.

4. RESULTS AND ANALYSIS

Figure 1 shows the detections of $\text{CH}_3\text{OCH}_2\text{OH}$ in the 0.2'' Band 7 data (black) toward MM1 convolved to the spectral resolution of the observations, and with a 2.4 km s⁻¹ linewidth (red). The position chosen for analysis (J2000 17:20:53.373, -35:46:58.14) lies ~ 400 au west of the brightest continuum peak, denoted MM1b by Brogan et al. (2016). The spectra were converted from Jy/beam to K intensity scale in each spectral window using the beam sizes listed in Table 1.

Table 1. Summary of ALMA observing parameters

Parameter	249 GHz	287 GHz	303 GHz	344 GHz
Observation date(s)	2017 Aug 18, 19	2016 Jul 18, 2016 Aug 02	2016 Jan 17	2016 Jul 17, 2016 Aug 02
Cycle: configuration(s)	4: C40-7	3: C36-4, C36-5	3: C36-2	3: C36-4, C36-5
Project code	2016.1.00383.S	2015.A.00022.T	2015.1.00150.S	2015.A.00022.T
Phase Center (J2000 RA, Dec)	17:20:53.30, −35:47:00.0	17:20:53.36, −35:47:00.0	17:20:53.35, −35:47:01.5	17:20:53.36, −35:47:00.0
Band	Band 6	Band 7	Band 7	Band 7
Time on Source (min)	37, 37	26, 26	27	27, 27
Number of antennas	42, 42	40, 39	40	38, 37
FWHP primary beam (″)	23	20	19	17
SPW center frequencies (GHz)	239.69, 241.16, 257.09, 258.29	280.1, 282.0, 292.1, 294.0	301.20, 302.00, 303.72	337.1, 339.0, 349.1, 351.0
Bandwidth per SPW (GHz)	4×0.9375	4×1.875	1.875, 1.875, 0.46875	4×1.875
Correlated channel width (MHz)	0.244, 0.488, 0.244, 0.244	0.977	0.488	0.977
Bandpass calibrator	J1924-2914	J1924-2914, J1517-2422	J1924-2914	J1924-2914
Gain calibrator	J1733-3722	J1717-3342	J1717-3342	J1717-3342
Flux calibrator	J1733-1304, J1617-5848	J1733-1304	J1733-1304	J1733-1304
Angular Resolution (″ × ″ (P.A.°))	0.11×0.08 (+76)	0.25×0.19 (−82)	0.87×0.64 (+74)	0.22×0.17 (−76)
Spectral Resolution (km s ^{−1})	0.6	1.1	1.0	1.1
RMS per channel (mJy beam ^{−1} (K)) ^a	1.1 (2.5)	2.0 (0.62)	20.0 (0.48)	3.3 (0.91)

^a The rms noise per channel varies significantly depending on whether bright emission is present in a particular channel, these estimated noise levels are the average of several channels, and several off-source locations in channels with moderate line emission present.

Also shown is a total simulation in green of the major contributors to the line density in these portions of the spectrum: methyl cyanide (CH₃CN) $v_8=0,1$, CH₃OH $v_t=0,1$, methyl formate (CH₃OCHO) $v_t=0,1$, ethanol (CH₃CH₂OH), g′Ga-ethylene glycol (g′Ga-(CH₂OH)₂), and g′Gg-(CH₂OH)₂, the latter of which has only recently been detected for the first time in the ISM (Jørgensen et al. 2016). Emission from many of the lines of these species is optically-thick, and a correction was applied using the formalisms of Goldsmith & Langer (1999) and Turner (1991).

This Band 7 data contained the largest number of unblended features, and so was chosen for a preliminary excitation and column density analysis. Given the RMS noise of the observations, the somewhat significant uncertainty introduced by the continuum subtraction due to the lack of line-free channels, and the extremely large spectral dynamic range, only features at least 10σ above the RMS, and not substantially blended with another spectral feature, were considered significant enough to be claimed as a detected line.

The underlying substructure of the methyl rotor-split transitions results in challenging, non-Gaussian line profiles which made it difficult to extract physically-meaningful quantitative results from a rotation diagram analysis. Instead, the convolved spectra were simulated using a single-excitation model following the formalism

established in Hollis et al. (2004):

$$N_T = \frac{Qe^{E_u/T_{ex}}}{\frac{8\pi^3}{3k}\nu S\mu^2} \times \frac{\frac{1}{2}\sqrt{\frac{\pi}{\ln(2)}}\frac{\Delta T_A \Delta V}{\eta_B}}{1 - \frac{e^{h\nu/kT_{ex}} - 1}{e^{h\nu/kT_{bg}} - 1}} \quad (5)$$

where N_T is the column density (cm^{−2}), E_u is the upper state energy (K), $\Delta T_A \Delta V$ is integrated line intensity (K cm s^{−1}), T_{ex} is the excitation temperature (K), T_{bg} is the background continuum temperature (~ 53 K at 287 GHz and ~ 66 K at 344 GHz), ν the transition frequency (Hz), S is the intrinsic line strength, μ^2 is the transition dipole moment (Debye²)¹, and η_B is the beam efficiency (assumed to be unity for these interferometric observations). The rotational partition function, Q_{rot} , is calculated explicitly by direct summation of states ($Q_{rot}[300 \text{ K}] = 81794$); the vibrational partition function correction, Q_{vib} , was obtained from quantum chemical calculations ($Q_{vib}[300 \text{ K}] = 5.33$; see Appendix B). We assume that the source fills the beam. The excitation temperature was fixed to 200 K, and the column density was varied to minimize the RMS intensity error for unblended transitions. A few of the strongest lines are marginally affected by optical depth, and a correction was applied using the formalisms of Goldsmith & Langer (1999) and Turner (1991). The final derived

¹ These units must be properly converted to Joules·cm³ to give N_T in cm^{−2}.

value is $N_T = 4(2) \times 10^{18} \text{ cm}^{-2}$ at $T_{ex} = 200 \text{ K}$. The $\sim 60\%$ uncertainty in the column density is taken as a contribution of 30% resulting from the fit to the unblended transitions, and an estimated 50% from the assumed excitation temperature, added in quadrature.

Further unblended transitions were identified in the 0.1'' Band 6 and 1'' Band 7 datasets toward MM1 (Figure 2). The simulated profiles of $\text{CH}_3\text{OCH}_2\text{OH}$ in the Band 6 data were made using the same values of N_T , T_{ex} , and ΔV as the 0.2'' Band 7 data, and with T_{bg} values appropriate for the data ($\sim 32 \text{ K}$). Because these profiles show remarkably good agreement even at twice the spatial resolution, this is likely indicating that the two observations are probing the same gas, and that the distribution is at least mostly resolved. The 1'' Band 7 data required a column density a factor of two lower, and substantially more optically thin, in agreement with a larger beam which did not resolve the substructure seen in the higher-resolution observations. In total, more than two dozen largely unblended transitions were identified in the datasets for which a distinguishable line-shape contribution was seen in the spectrum matching the predicted shape at the correct frequency. As noted earlier, the intensity match is not always precise, due to the uncertainty in the excitation temperature.

4.1. Spatial Distributions

The line density in the region is such that it is challenging to select transitions which are not blended from which spatial distributions can be inferred. Figure 3 shows integrated intensity images of three unblended $\text{CH}_3\text{OCH}_2\text{OH}$ transitions (panels a-c), as well as images of a single unblended transition each of $\text{a'Gg}-(\text{CH}_2\text{OH})_2$, CH_3CN , and $^{13}\text{CH}_3\text{OH } v_t=1$. The $\text{CH}_3\text{OCH}_2\text{OH}$ transitions show nearly identical spatial distributions to each other, as expected, and markedly different distributions from $\text{g'Gg}-(\text{CH}_2\text{OH})_2$, which is significantly more compact, as well as CH_3CN which, especially in MM2, shows an anti-correlated distribution. Notably, the distribution of $\text{CH}_3\text{OCH}_2\text{OH}$ appears to be similar to, but slightly more compact than, that of $^{13}\text{CH}_3\text{OH } v_t=1$. The ring-like appearance of the molecular emission toward MM1 is due to the high dust continuum opacity (> 1) and brightness temperature of the 1 mm dust continuum emission toward the dust peaks ($> 100 \text{ K}$ Brogan et al. 2016). Toward the continuum peaks, the high dust opacity attenuates the line emission from the backside of the region, and the high background continuum brightness temperature compared to the line excitation temperature of the transitions shown here (of order 100-200 K) leads to weaker line emission (lower excitation lines are seen in absorption against the con-

tinuum peaks). To mitigate these effects, the spectra were extracted and analyzed at a position offset from the continuum peak.

4.2. Chemical Modeling

$\text{CH}_3\text{OCH}_2\text{OH}$ was included in the three-phase chemical kinetics model *MAGICKAL* of Garrod (2013). In an initial effort to explore the ability of the model to reproduce the observed abundance, we modified the model with the back-diffusion correction of Willis & Garrod (2017), and used a network based on that of Belloche et al. (2017), in which $\text{CH}_3\text{OCH}_2\text{OH}$ is produced via Reaction 4. The network also contains likely gas-phase and grain-surface destruction mechanisms for $\text{CH}_3\text{OCH}_2\text{OH}$.

The chemical modeling was performed using the two-stage approach described in Garrod (2013). Phase 1 is a cold collapse to a maximum density of $2 \times 10^8 \text{ cm}^{-3}$ and a dust grain temperature of 8 K. This is followed by a warm-up from 8 K to 400 K, simulating the ‘ignition’ of a hot core. Three different warm-up timescales have been used, as the choice of timescale has been previously shown to have significant effects on the chemistry (Garrod 2013). The fastest timescale reaches a temperature of 200 K at $5 \times 10^4 \text{ yr}$, and 400 K at $7.12 \times 10^4 \text{ yr}$. The slowest timescale reaches these milestones at 10^6 yr and $1.43 \times 10^6 \text{ yr}$; the intermediate timescale takes $2 \times 10^5 \text{ yr}$ and $2.85 \times 10^5 \text{ yr}$.

The results of the model are shown graphically in Figure 4. The fast warm-up timescale produces the highest abundance of $\text{CH}_3\text{OCH}_2\text{OH}$, with a maximum fractional abundance of $\sim 10^{-12}$ with respect to total hydrogen, which is well-maintained to a temperature of 400 K. The abundance of CH_3OH in the same model approaches 10^{-5} , corresponding to $\text{CH}_3\text{OCH}_2\text{OH}:\text{CH}_3\text{OH}$ of $\sim 10^{-7}$. The observed ratio of $\text{CH}_3\text{OCH}_2\text{OH}:\text{CH}_3\text{OH}$ is estimated to be 1:34 (see Appendix C). The intermediate timescale shows very similar results, while the slowest timescale produces a very low gas-phase abundance of $\text{CH}_3\text{OCH}_2\text{OH}$, peaking at $\sim 10^{-17}$. This is due to the increased efficiency of grain-surface destruction mechanisms in the slow warm-up timescale.

5. DISCUSSION

Most complex organic molecules (COMs), especially saturated species, are thought to have efficient formation pathways in the solid-phase on the surface of dust grains (Garrod et al. 2008). In star-forming regions like NGC 6334I, the gradual warm-up of these grains can then thermally desorb the product molecules into the gas phase, where they are detected by radio observations

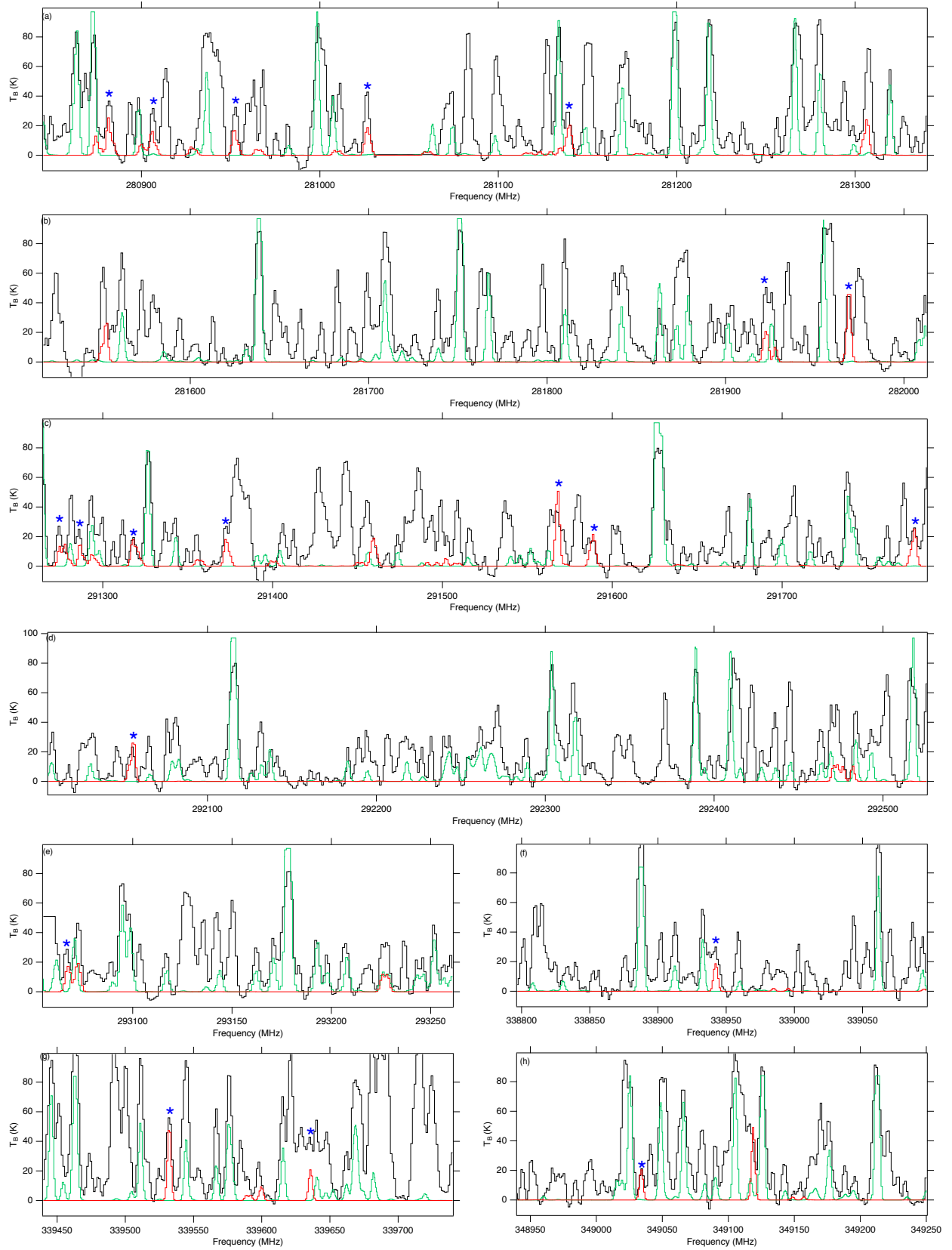


Figure 1. Band 7 spectrum of NGC 6334I extracted toward the MM1 core at $0.2''$ resolution in black, and adjusted to a $v_{lsr} = -7 \text{ km s}^{-1}$. Single-excitation temperature model spectra of $\text{CH}_3\text{OCH}_2\text{OH}$ at $T_{ex} = 200 \text{ K}$, $\Delta V = 2.4 \text{ km s}^{-1}$, and $N_T = 4(2) \times 10^{18} \text{ cm}^{-2}$ are overlaid in red. In green are simulations of the species that are major contributors to the line density in these windows (see text §4). Transitions of $\text{CH}_3\text{OCH}_2\text{OH}$ that are largely unblended (have distinguishable lineshapes) are marked with blue asterisks.

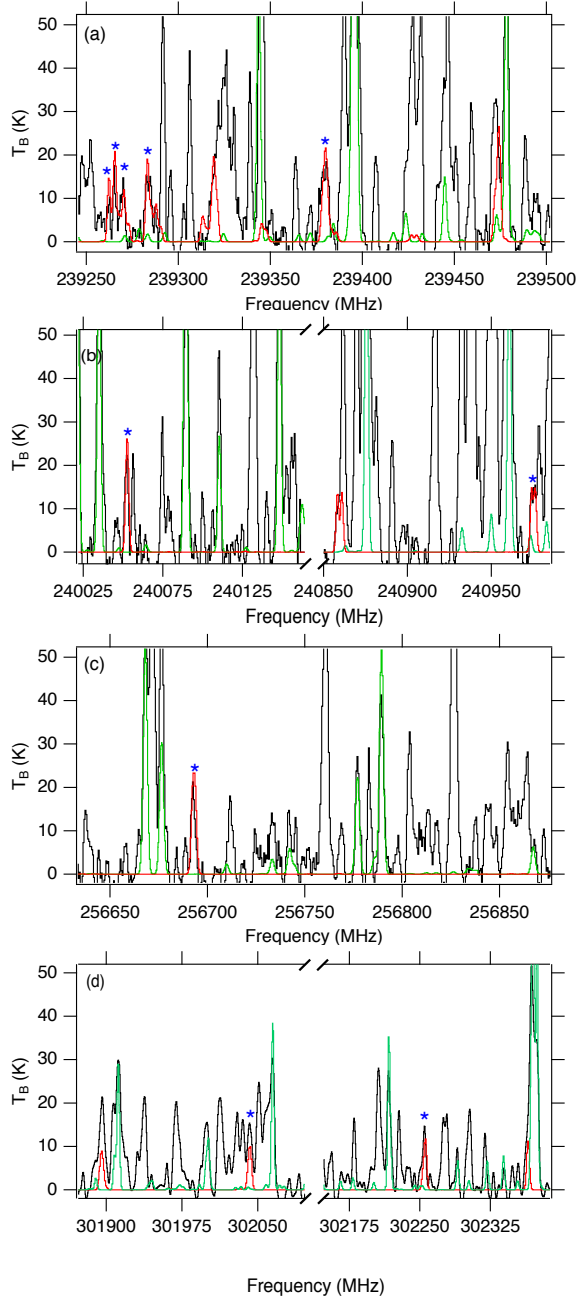
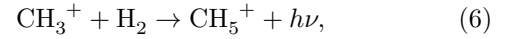


Figure 2. Detections of $\text{CH}_3\text{OCH}_2\text{OH}$ indicated in red are overlaid on spectra of NGC 6334I toward MM1 in Band 6 ($0.1''$; panels a-c) and Band 7 ($1''$; panel d) in black. The Band 6 data were adjusted to a $v_{lsr} = -7 \text{ km s}^{-1}$, while the Band 7 data were adjusted to a $v_{lsr} = -8 \text{ km s}^{-1}$ due to the different gas being probed by the larger beam. $\text{CH}_3\text{OCH}_2\text{OH}$ simulations are at $T_{ex} = 200 \text{ K}$, $\Delta V = 2.4 \text{ km s}^{-1}$ in both datasets, with $N_T(\text{Band 6}) = 4(2) \times 10^{18} \text{ cm}^{-2}$ and $N_T(\text{Band 7}) = 2 \times 10^{18} \text{ cm}^{-2}$. In green are simulations of the species that are major contributors to the line density in these windows (see text §4). Transitions of $\text{CH}_3\text{OCH}_2\text{OH}$ that are largely unblended (have distinguishable lineshapes) are marked with blue asterisks.

(Garrod 2013). For instance, the successive hydrogenation of CO on grains is likely the major formation route for methanol (Watanabe & Kouchi 2002; Fuchs et al. 2009). Yet, other studies have shown that some saturated COMs, such as methyl formate and formamide (NH_2CHO), might have significant, if perhaps not dominant, gas-phase formation pathways (Neill et al. 2012; Codella et al. 2017). It is worthwhile, then, to consider the potential operative pathways, both in the gas- and solid-phase, for the formation of $\text{CH}_3\text{OCH}_2\text{OH}$.

5.1. Radical-Radical Recombination

As noted by Motiyenko et al. (2017), the most obvious astrochemically relevant formation mechanism is the association of the CH_3O and CH_2OH radicals, which can occur on grains or in the gas. In the gas phase, an association reaction occurs via an intermediate complex, which re-dissociates into reactants unless it can relax sufficiently rapidly. In the low density interstellar medium, the relaxation mechanism is radiative, typically via emission from vibrational levels above the energy of reactants to levels below this energy and therefore stable. For ion-neutral systems such as



experiments in ion traps and other low-density devices have been performed and show a wide range of reaction rate coefficients, depending upon the depth of the complex potential well (which helps to determine the lifetime of the complex against dissociation), the size of the reactants, and the temperature (Gerlich & Horning 1992). The experiments have also been supplemented by statistical calculations (e.g. Herbst 1985).

Both approaches show that a large complex well depth (a few eV), large reactants (more than 4-5 atoms), and low temperatures ($< 100 \text{ K}$) are needed for the radiative rate coefficient to approach the collisional rate coefficient, and make these reactions feasible. Without these constraints, much smaller rate coefficients are obtained.

For neutral-neutral systems, very few reactions have been studied in the laboratory. Some theoretical rate coefficients have been obtained via statistical theories (Vuitton et al. 2011); these indicate indirectly that the association of the CH_3O and CH_2OH radicals might have a large rate coefficient at temperatures under 100 K , although it is also likely that the low gas-phase abundances of the reactants would render the process inefficient even with a large rate coefficient. Thus, if the radicals CH_3O and CH_2OH are more abundant on grains than in the gas for large ranges of temperature, the solid-phase association should be the more important. On the other hand, in their gas-grain modeling of the formation of CH_3OCH_3 in cold clouds, Balucani et al. (2015)

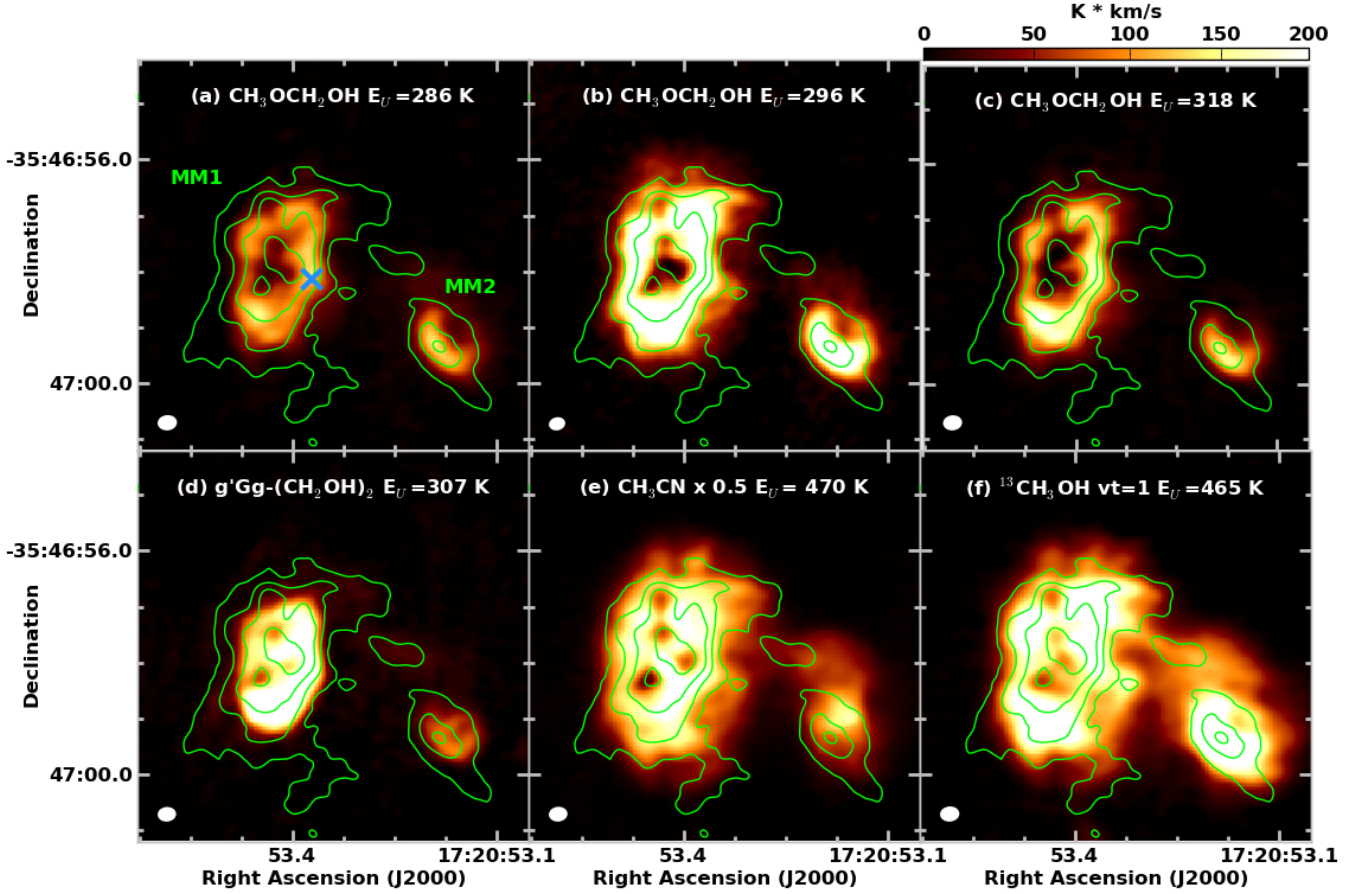


Figure 3. Moment 0 maps of three $\text{CH}_3\text{OCH}_2\text{OH}$ transitions (panels *a-c*) compared to those of $\text{a'Gg}-(\text{CH}_2\text{OH})_2$, CH_3CN , and $^{13}\text{CH}_3\text{OH } v_t=1$, with the 1 mm continuum overlaid as green contours (levels are 18, 53, 140, and 370 mJy beam^{-1}). The pertinent transition parameters for these lines are given in Table A1 and the Supplementary Information. The blue cross in panel (a) indicates the position from which spectra were extracted toward MM1, and the synthesized beams are shown in the lower left of each panel in white.

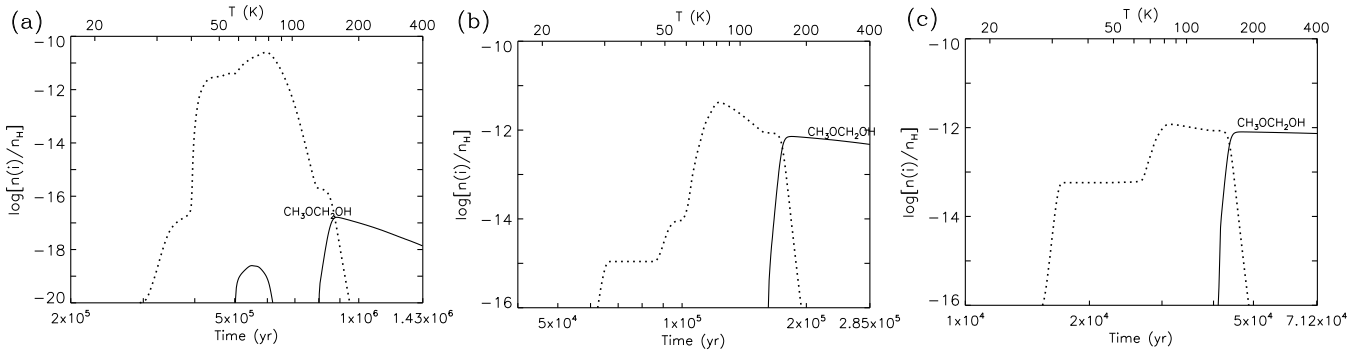


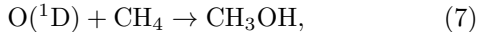
Figure 4. Abundance profiles of $\text{CH}_3\text{OCH}_2\text{OH}$ for three warm-up timescales. Gas-phase abundance is displayed as a solid curve, while grain-surface abundance is shown as a dotted curve. Panel (a) shows the abundance profile for the longest warm-up timescale; (b) and (c) show the abundance profile for the intermediate and fast warm-up timescales, respectively.

found the dominant process to be the gas-phase radiative association between CH_3 and CH_3O , assuming that it occurred at the collisional rate.

5.2. $\text{O}(^1\text{D})$ Insertion Reactions

Another possible formation route involves the insertion of $\text{O}(^1\text{D})$ into one of the C-H bonds of CH_3OCH_3 (Hays & Widicus Weaver 2013). Electronically excited species like $\text{O}(^1\text{D})$ can form in cosmic ray-irradiated dust-grain ice-mantles, where they quickly react with a

neighboring species or are quenched by the solid (Shingledecker et al. 2017; Shingledecker & Herbst 2017). Indeed, Bergner et al. (2017) recently found evidence that an analogous reaction,



could occur efficiently in interstellar ices. It is possible that such excited species could also react in the gas-phase in the ISM, however, it is perhaps more likely that the excited species will emit a photon and radiatively relax before encountering a collisional reaction partner in the gas phase.

5.3. Photodissociation vs Cosmic Rays

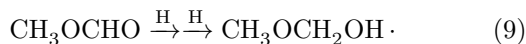
As mentioned in §1, both CH_3O and CH_2OH can be formed from the dissociation of methanol. In the ISM, the two main drivers of dissociation are photons and cosmic rays. As recently noted by Shingledecker & Herbst (2017), the products of photochemistry and radiation chemistry are often similar, but not necessarily identical, due to differences in the underlying microscopic interactions that drive such processes. The distinction between photochemistry and radiation chemistry is potentially of importance for $\text{CH}_3\text{OCH}_2\text{OH}$, and was noted by Boamah et al. (2014) and Sullivan et al. (2016). In the experiments described in those works, $\text{CH}_3\text{OCH}_2\text{OH}$ was detected after the exposure of condensed methanol to low-energy (<20 eV) electrons, which are characteristic of the secondary electrons produced in interstellar ices due to cosmic ray bombardment (Shingledecker et al. 2017). In photodissociation experiments, however, $\text{CH}_3\text{OCH}_2\text{OH}$ was not detected as a product of UV-irradiated methanol ice, which Sullivan et al. (2016) indicate might make $\text{CH}_3\text{OCH}_2\text{OH}$ a good tracer of cosmic ray-induced chemistry in the ISM.

5.4. Grain-Surface Hydrogenation

Yet another potential formation pathway is through hydrogenation of precursor species on grain surfaces, such as:



or



Successive hydrogenation reactions have been proposed as the formation mechanism for a number of saturated species, including CH_3OH (Woon 2002) and NH_2OH (Fedoseev et al. 2016) among numerous others Linnartz et al. (2015), although recent work has suggested this may not be efficient for substituted aldehydes (Jonusas et al. 2017). A more in-depth analysis of the potential of these types of reactions to both form $\text{CH}_3\text{OCH}_2\text{OH}$ and suggest other potential products, is warranted.

5.5. Comparison to Models

As discussed in §4.2, current models using only Reaction 4 are significantly under-producing $\text{CH}_3\text{OCH}_2\text{OH}$. While the derived abundance of CH_3OH in our observations has a high degree of uncertainty, it is clear that the current models do not properly treat $\text{CH}_3\text{OCH}_2\text{OH}$ formation, destruction, or both. Yet, as shown in Figure 3, the $\text{CH}_3\text{OCH}_2\text{OH}$ distribution is remarkably similar to that of CH_3OH , and different from other COMs. While not definitive, this is highly suggestive of a closely-tied chemistry between these two species that would favor Reaction 4.

6. CONCLUSIONS

We have reported the detection of methoxymethanol $\text{CH}_3\text{OCH}_2\text{OH}$ for the first time in the ISM using ALMA Bands 6 and 7 observations toward the massive Galactic protocluster NGC 6334I. More than two dozen unblended transitions above 10σ were identified. These transitions show identical spatial distributions, distinct from other complex species, and well-matched to that of CH_3OH , a likely precursor. Current treatments for the grain-surface formation of $\text{CH}_3\text{OCH}_2\text{OH}$ from CH_3O and CH_2OH significantly under-produce $\text{CH}_3\text{OCH}_2\text{OH}$, likely indicating other unconsidered formation pathways exist. Further, as has recently been suggested, cosmic ray-induced chemistry may play a substantial role, making $\text{CH}_3\text{OCH}_2\text{OH}$ a potentially powerful tracer of this process.

This paper makes use of the following ALMA data: ADS/JAO.ALMA#2015.A.00022.T, ADS/JAO.ALMA#2015.1.00150.S, and ADS/JAO.ALMA#2016.1.00383.S. ALMA is a partnership of ESO (representing its member states), NSF (USA) and NINS (Japan), together with NRC (Canada) and NSC and ASIAA (Taiwan) and KASI (Republic of Korea), in cooperation with the Republic of Chile. The Joint ALMA Observatory is operated by ESO, AUI/NRAO and NAOJ. The National Radio Astronomy Observatory is a facility of the National Science Foundation operated under cooperative agreement by Associated Universities, Inc. E. H. thanks the National Science Foundation for support of his astrochemistry program. A.M.B. is a Grote Reber Fellow, and support for this work was provided by the NSF through the Grote Reber Fellowship Program administered by Associated Universities, Inc./National Radio Astronomy Observatory. Support for B.A.M. was provided by NASA through Hubble Fellowship grant #HST-HF2-51396 awarded by the Space Telescope Science Institute, which is operated by the Association of Universities for Research in As-

tronomy, Inc., for NASA, under contract NAS5-26555. This work was supported by the Programme National “Physique et Chimie du Milieu Interstellaire” (PCMI)

of CNRS/INSU with INC/INP co-funded by CEA and CNES.

REFERENCES

- Balucani, N., Ceccarelli, C., & Taquet, V. 2015, *MNRAS*, 449, L16
- Belloche, A., Meshcheryakov, A. A., Garrod, R. T., et al. 2017, *A&A*, 601, A49
- Bergner, J. B., Öberg, K. I., & Rajappan, M. 2017, *ApJ*, 845, 29.
- Boamah, M. D., Sullivan, K. K., Shulenberger, K. E., et al. 2014, *Faraday Discussions*, 168, 249.
- Brogan, C. L., Hunter, T. R., Cyganowski, C. J., et al. 2016, *ApJ*, 832, 1
- Cernicharo, J., Marcelino, N., Roueff, E., et al. 2012, *ApJ*, 759, L43
- Codella, C., Ceccarelli, C., Caselli, P., et al. 2017, *A&A*, 605, L3
- Fedoseev, G., Chuang, K. J., van Dishoeck, E. F., Ioppolo, S., & Linnartz, H. 2016, *MNRAS*, 460, 4297
- Frisch, M., Trucks, G., Schlegel, H., et al. 2009, *Gaussian 09*, Revision B.01, Gaussian, Inc., Wallingford CT
- Fuchs, G. W., Cuppen, H. M., Ioppolo, S., et al. 2009, *A&A*, 505, 629
- Garrod, R. T. 2013, *ApJ*, 765, 60
- Garrod, R. T., Weaver, S. L. W., & Herbst, E. 2008, *ApJ*, 682, 283
- Gerlich, D., & Horning, S. 1992, *Chem Rev*, 92, 1509
- Goldsmith, P.F. & Langer, W.D. 1999, *ApJ*, 517, 209.
- Hays, B. M., & Widicus Weaver, S. L. 2013, *JPCA*, 117, 7142
- Herbst, E. 1985, *ApJ*, 291, 226
- Hollis, J. M., Jewell, P. R., Lovas, F. J., & Remijan, A. 2004, *ApJ*, 613, L45
- Hunter, T. R., Brogan, C. L., Megeath, S. T., et al. 2006, *ApJ*, 649, 888
- Hunter, T. R., Brogan, C. L., MacLeod, G., et al. 2017, *ApJL*, 837, L29
- Jonusas, M., Guillemin, J.-C., & Krim, L. 2017, *MNRAS*, 468, 4592.
- Jørgensen, J. K., van der Wiel, M., Coutens, A., et al. 2016, *A&A*, 595, A117
- Laas, J. C., Garrod, R. T., Herbst, E., & Widicus Weaver, S. L. 2011, *ApJ*, 728, 71
- Laas, J. C., Hays, B. M., & Widicus Weaver, S. L. 2013, *JPCA*, 117, 9548
- Linnartz, H., Ioppolo, S., & Fedoseev, G. 2015, *International Reviews in Physical Chemistry*, 34, 205
- Milam, S. N., Savage, C., Brewster, M. A., Ziurys, L. M., & Wyckoff, S. 2005, *ApJ*, 634, 1126
- Motiyenko, R., Margules, L., Despois, D., & Guillemin, J.-C. 2017, *PCCP*, in press, doi:10.1039/c7cp05932a.
- Neill, J. L., Muckle, M. T., Zaleski, D. P., et al. 2012, *ApJ*, 755, 153
- Reid, M. J., Menten, K. M., Brunthaler, A., et al. 2014, *ApJ*, 783, 130
- Shingledecker, C. N., & Herbst, E. 2017, *Phys. Chem. Chem. Phys.*, in press, doi:10.1039/C7CP05901A.
- Shingledecker, C. N., Le Gal, R., & Herbst, E. 2017, *Phys. Chem. Chem. Phys.*, 19, 11043.
- Sullivan, K. K., Boamah, M. D., Shulenberger, K. E., et al. 2016, *MNRAS*, 460, 664.
- Turner, B.E. 1991, *ApJS*, 76, 617.
- Vuitton, V., Yelle, R. V., Lavvas, P., & Klippenstein, S. J. 2011, *ApJ*, 744, 11
- Watanabe, N., & Kouchi, A. 2002, *ApJL*, 571, L173
- Willis, E. R., & Garrod, R. T. 2017, *ApJ*, 840, 61
- Woon, D. E. 2002, *ApJ*, 569, 541
- Zernickel, A., Schilke, P., Schmiedeke, A., et al. 2012, *A&A*, 546, A87

APPENDIX

A. OBSERVED LINE PARAMETERS

Table A1. Pertinent line parameters of selected observed $\text{CH}_3\text{OCH}_2\text{OH}$, $\text{g}'\text{Gg}-(\text{CH}_2\text{OH})_2$, CH_3CN , and $^{13}\text{CH}_3\text{OH } v_t=1$ transitions.

Quantum Numbers	Frequency (MHz)	$S_{ij}\mu^2$ (Debye ²)	E_u (K)
$\text{CH}_3\text{OCH}_2\text{OH}$			
$27_{12,15} - 26_{12,14} \text{ E}$	281024.6590	1.05	271.81
$27_{12,16} - 26_{12,15} \text{ A}$	281026.0480	1.05	271.81
$27_{12,15} - 26_{12,14} \text{ A}$	281026.0480	1.05	271.81
$27_{12,16} - 26_{12,15} \text{ E}$	281027.8190	1.05	271.81
$\text{g}'\text{Gg}-(\text{CH}_2\text{OH})_2^\dagger$			
$28_{15,13} - 28_{14,14} v_t=1$	292703.3917	199.61	307.44
$28_{15,14} - 28_{14,15} v_t=1$	292703.3917	155.24	307.44
CH_3CN			
$16_7 - 15_7$	294.02549	274.21	469.79
$^{13}\text{CH}_3\text{OH } v_t=1$			
$6_{3,4} - 5_{3,3}$	282383.0330	3.64	465

[†] Here, v_t refers to a large-amplitude tunneling motion of the OH moieties.

NOTE—Only a sample of the $\text{CH}_3\text{OCH}_2\text{OH}$ transitions is shown here; the full table of all transitions within the range of these observations is available as Supplementary Information.

B. $\text{CH}_3\text{OCH}_2\text{OH}$ VIBRATIONAL PARTITION FUNCTION

The vibrational correction to the partition function for $\text{CH}_3\text{OCH}_2\text{OH}$ was calculated according to Equation A1:

$$Q(T)_{vib} = \prod_{i=1}^{3N-6} \frac{1}{1 - e^{-E_i/kT}}. \quad (\text{A1})$$

To obtain the vibrational energy levels for $\text{CH}_3\text{OCH}_2\text{OH}$, a geometry optimization and frequency analysis was performed using Gaussian 09 (Frisch et al. 2009) at the B3LYP/6-311++G(d,p) level of theory and basis set. The five lowest energy levels contribute >0.1% correction to the partition function at 200 K, and have energies of 139, 188, 360, 396, and 584 cm^{-1} . The total correction at 200 K is 2.49.

C. CH_3OH COLUMN DENSITY

To compare with the column density of $\text{CH}_3\text{OCH}_2\text{OH}$, a column density estimate of CH_3OH was required. In the 0.2'' Band 7 data, nearly every CH_3OH transition is

optically thick, as is nearly every transition of $^{13}\text{CH}_3\text{OH}$. The lines of $^{13}\text{CH}_3\text{OH } v_t=1$ are, however, largely optically thin (see Figure A1). We assume that the $v_t=0$ and $v_t=1$ states of $^{13}\text{CH}_3\text{OH}$ are described by a single excitation temperature, and calculate a total column density of $^{13}\text{CH}_3\text{OH}$ using the $6_{3,4} - 5_{3,3}$ transition at 282383 MHz, which appears to be the least blended optically thin line. A background temperature of $T_{bg} = 53$ K was used, and an excitation temperature of $T_{ex} = 150$ K, based on the background temperature and the brightness temperature of the optically thick $^{13}\text{CH}_3\text{OH}$ lines. The partition function included contributions from both $v_t=0$ and $v_t=1$. A linewidth of 2.8 km s^{-1} was fit to the lines. The resulting column density was $N_T = 1.95 \times 10^{18} \text{ cm}^{-2}$. A CH_3OH column density of $N_T = 1.4 \times 10^{20} \text{ cm}^{-2}$ was then inferred by scaling by a $^{12}\text{C}/^{13}\text{C}$ ratio of 68 (Milam et al. 2005). Given the uncertainties involved and assumptions made, this value should be viewed as an estimate and as a lower limit.

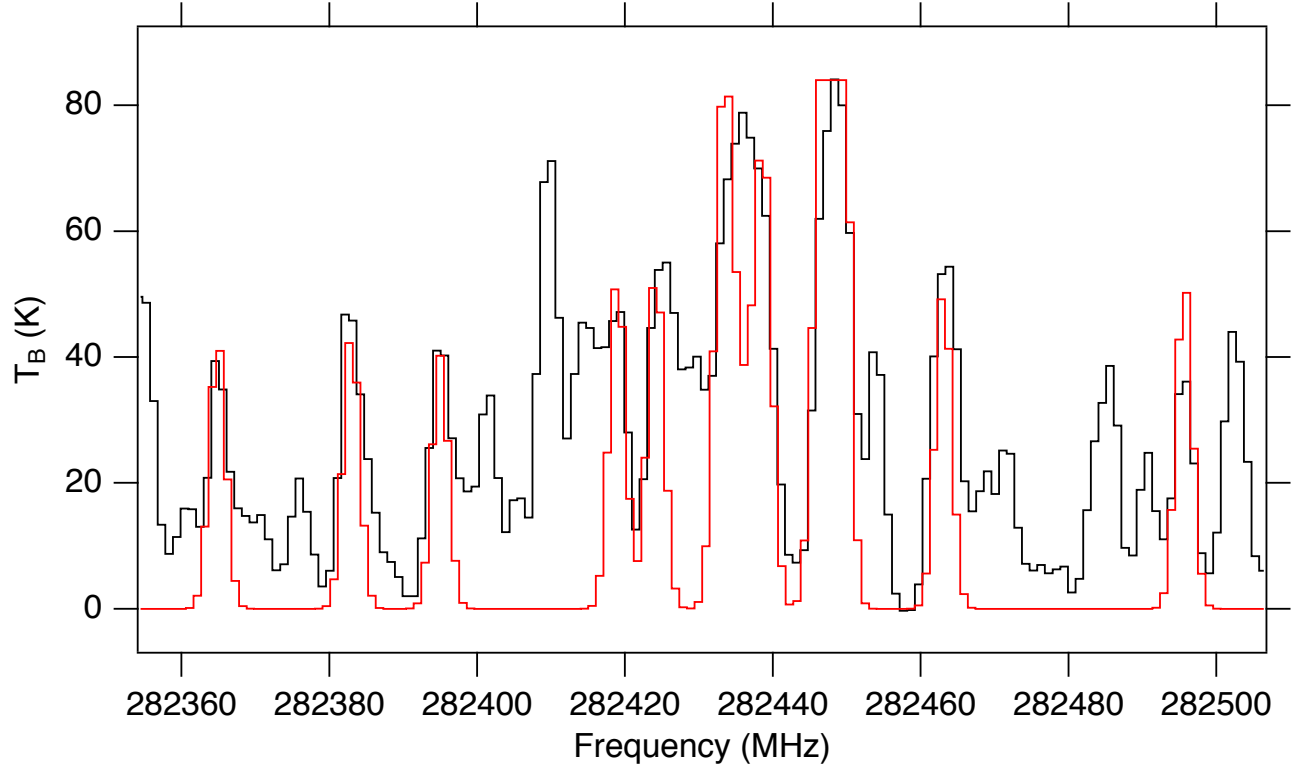


Figure A1. Simulation of $^{13}\text{CH}_3\text{OH } v_t=1$ in red over observations of MM1 in black with $N_T = 1.95 \times 10^{18} \text{ cm}^{-2}$, $T_{ex} = 150 \text{ K}$, and $\Delta V = 2.8 \text{ km s}^{-1}$.